66 relationship between brain atrophy and HbA1c in elderly diabetics should be
67 examined further in a prospective study.
68
69 ACKNOWLEDGMENT
70 We would like to express our appreciation to Professors Kamae and
71 Yanagisawa of Kobe University for their assistance with the statistical analysis.

REFERENCES

1. Araki Y, Nomura M, Tanaka H et al. MRI of the brain in diabetes mellitus. Neuroradiology 1994; 36:101-103.
2. Schmidt R, Launer L, Nilsson L et al. Magnetic resonance imaging of the brain in diabetes: the Cardiovascular Determinants of Dementia (CASCADE) Study. Diabetes 2004; 53: 687-692.
3. Soininen H, Puranen M, Helkala E et al. Diabetes mellitus and brain atrophy: A computed tomography study in an elderly population. Neurobiol. Aging 1992; 13: 717-721.
4. den Heijer T, Vermeer S, van Dijk E et al. Type 2 diabetes and atrophy of medial temporal lobe structures on brain MRI. Diabetologia 2003; 46:1604-1610.
5. Kuo H, Jones R, Milberg W et al. Effect of blood pressure and diabetes mellitus on cognitive and physical functions in older adults: a longitudinal analysis of the advanced cognitive training for independent and vital elderly cohort. J Am Geriatr Soc. 2005; 53:1154-1161.
6. The American psychiatric association. Diagnostic and statistical manual of mental disorders. 4th Ed (DSM-IV). Washington D.C.,1994.
7. Nicolas J, Estruth R, Salamero M et al. Brain impairment in well-nourished chronic alcoholics related to ethanol intake. Ann. Neurol 1997; 41: 591-598.
8. Kahn CH, Weir GC, King GL et al. Joslin's Diabetes Mellitus. Boston: Joslin Diabetes Center, 2005.
9. Enzinger C, Fazakas F, Matthews PM et al. Risk factors for progression of brain atrophy in aging. Six-year follow-up of normal subjects. Neurology 2005; 64: 1704-1711.
10. Cardenas VA, Du AT, Hardin D et al. Comparison of methods for measuring longitudinal brain change in cognitive impairment and dementia. Neurobiol Aging 2003; 24: 537-544.

Table 1. Clinical characteristics of control and diabetic subjects

	Control	Diabetes	P value
Number	48	67	
Age (years)	68.7±0.9	70.0±0.8	0.267*
Men (%)	23 (47.9)	24 (35.8)	0.193¶
BMI (kg/m^2)	20.6±0.4	26.2±0.4	0.001*
MMSE score	-	26.3±0.3	-
Duration of diabetes (years)	-	18.1±1.1	-
Fasting blood glucose (mg/dl)	94.9±0.9	164.8±9.6	0.015*
HbA1c (%)	5.2±0.1	8.1±0.2	<0.001*
Total-cholesterol (mg/dl)	198.4±4.6	214.7±5.0	0.292*
Triglyceride (mg/dl)	107.8±7.3	124.2±7.1	0.452*
HDL-cholesterol (mg/dl)	-	63.6±2.8	-
Insulin use (%)	-	38 (56.7)	-
Systolic blood pressure (mmHg)	110.3±1.9	135.1±2.6*	0.001*
Diastolic blood pressure (mmHg)	65.0±1.3	73.9±1.1*	0.009*
Diabetic retinopathy (%)	-	44 (65.7)	-
Symptomatic nephropathy (%)	-	37 (55.2)	-
Persistent proteinuria (%)	-	21 (31.3)	-
Coronary artery disease (%)	-	24 (35.8)	-

Data are given as means ± standard error or percentage.

*Mann-Whitney U test, ¶χ^2 test. BMI, body mass index; MMSE, mini-mental state test examination

Impaired response of perforating arteries to hypercapnia in chronic hyperglycemia

Ximena-Sayuri Oizumi [1], Taichi Akisaki [1], Yoshiyuki Kouta [1], Xiu Z. Song [1], Toshihiro Takata [1], Takeshi Kondoh [2], Keiji Umetani [3], Masatsugu Hirano [3], Katsuhito Yamasaki [3], Eiji Kohmura [2], Koichi Yokono [1] and Takashi Sakurai [1*]

[1] Department of Internal and Geriatric Medicine, Kobe University, Graduate School of Medicine, Kobe, Japan

[2] Department of Neurosurgery, Kobe University, Graduate School of Medicine, Kobe, Japan

[3] Japan Synchrotron Radiation Research Institute, Spring-8, Sayo-gun, Hyogo, Japan

*Corresponding author: Takashi Sakurai, M.D. Ph.D.,

Department of Internal and Geriatric Medicine, Kobe University Graduate School of Medicine, 7-5-1 Kusunoki-cho, Chuo-ku, Kobe 650-0017, Japan

Phone: + 81-78-382-5901

Fax: + 81-78-382-5919

Introduction

Diabetes mellitus involves long-term vascular complications and hyperglycemia is recognized as the main cause in the pathogenesis of these diabetic vasculopathies. In brain, diabetes increases the risks of large and small cerebrovascular diseases and makes patients demonstrably more susceptible to cerebral ischemia (Karapanayiotides). Hyperglycemia has been shown to increase neurologic deficits in models of hypoxic-ischemic-injury and it is possible that differences in the regulation of CBF could be responsible for this susceptibility (LeBlanc 1993).

Hypercapnia is a potent dilator of cerebral blood vessels, but the effects of hypercapnia on CBF and cerebrovascular reactivity during diabetes are still inconsistent. In human studies, impaired vascular responses to hypercapnia have been reported (dandona et al 1978, dandona 1979, Griffith 1987, kadoi 2003), while in animal experiments, it has been found that CBF responses to hypercapnia of cortical arterioles are comparable to normal animals (kontos 1990, cenic 2000, sieber 1993, kawata 1998, rodriguez 1993).

Perforating arteries are terminal vessels directly emerging from the main cerebral arteries and particularly important because these arteries supply blood to brain structures such as basal ganglia, thalamus and hippocampus that are frequently impaired in diabetes (Groot 2000). Distinctive branching pattern and higher intraluminal pressure of perforating artery may suggest the differential regulation of vascular reactivity from that of the pial arterioles. However, to our knowledge, there is not any report about the vascular response of perforating arteries in vivo. In this study, we used a newly developed microangiographic technique and investigated the vascular response to hypercapnia of rat perforating arteries. There fore, the goal of the study presented here was to identify the effects of chronic hyperglycemia on hypercapnia-induced vascular responses (endothelium-dependent vasodilatation) and nitric oxide (NO) donor-induced vascular responses (endothelium-independent) of perforating arteries and of the deeply located large cerebral arteries.

Methods

Experimental design and animal preparation

All experimental procedures were performed following the guidelines set for animal experiments by the Kobe University Graduate School of Medicine. Six months-old Male Wistar-Kyoto and Goto-Kakizaki (GK) rats weighing 400 g -

450 g and 300 g - 350 g, respectively, were used. Animal rooms were controlled for temperature (23 ℃), humidity (55%) and light (12 h light-dark cycles).
In order to investigate the effects of hypercapnia on cerebral vascular reactivity, we divided the experimental animals into two. The first group compromised control Wistar rats (n=13). The second group compromised genetically diabetic GK rats (CLEA, Tokyo, Japan). For the hypercapnic challenge rats inhaled CO_2 at 12% mixed in air for 5 min. Then rats were allowed to a 15 min period of recovery under normal capnia. To investigate the endothelium-independent vascular vasodilatation we applied sodium nitroprusside (0.5 ug.kg -1.min-1, i.v.).

Microangiography and image analysis

Microangiographic imaging of the rat brain was performed at the third generation synchrotron radiation facility SPring-8 in Hyogo, Japan. The experimental arrangement for X-ray imaging using monochromatic synchrotron radiation X-rays at the SPring-8 BL20B2 beamline has been fully described elsewhere (umetani 1, umetani2). In brief, we used monochromatic synchrotron radiation as an X-ray source, which was obtained from an 8 GeV electron storage ring (Beamline BL20B2, SPring-8, Hyogo, Japan). X-Ray was monochromatized at 17 keV energy using a silicon double-crystal monochromator. The camera head incorporates an X-ray direct-sensing pick-up tube (Saticon). Absorbed X-rays in the photoconductive layer of the tube are directly converted into electron-hole pairs, and signal charges are read out by electron beam scanning. The digital images were acquired as 1024×1024 pixels with 10-bit resolution after analog-to-digital conversion. The field of view was 9×9 mm^2 and thus the pixel size was approximately 9 μm.
Under anesthesia (pentobarbital sodium, 50 mg/kg i.p.), rats were placed in the supine position in a stereotaxic frame with a window of 3 cm x 4 cm in the center of the platform for direct radiation of the head. After tracheotomy, each animal received pancuronium bromide (0.8 μ mol/kg) and was mechanically ventilated with room air using a ventilator (SAR 830/P ventilator, California, U.S.A.) at a rate of 60-70 respirations/min. One femoral artery and one femoral vein were cannulated with PE-50 tubing (Natsume Manufacturing, Tokyo, Japan). The artery line was to measure systemic arterial blood pressure using a disposable pressure monitoring kit (Life Kit, Nihon Kohden, Tokyo, Japan) connected to a computer (Unique Acquisition, Unique Medical Company, Osaka, Japan). A femoral vein catheter was implanted for drug administration. Rectal

temperature was maintained at 36-37 ℃ with a heating pad. The right external carotid artery (ECA) was cannulated. The PE-50 tube inserted was connected to an automated injector (Auto Injector 120S, Nihon Kohden, Tokyo, Japan) that was programmed to reproducibly deliver 0.2 ml of nonionic contrast media (Iomeprol, Daiichi Pharmaceutical Company, Tokyo, Japan) in 0.4 second for each microangiographic imaging.

For consistent measurement of the vascular diameters of these arteries, we established an exact measuring point for each vessel. For the measurement of the ICA, we chose a point at a distance of 665 um from the posterior communicating artery (Pcom), for MCA, a point at a distance of 475 um distant from the ICA bifurcation. Because perforating arteries have many anatomical variations in number and origin of the vessels (rieke 1981), we selected the largest branches emerging from the MCA and determined a measuring point at 190 – 380 um distant from the MCA for each of the perforating arteries. Measurements of vessel diameters after repetitive angiography were made consistently at the same point. On the stored digital images, vessel diameters were measured semi automatically with a software (Image-Pro Plus ver.4.0, Media Cybernetics Inc., Silver Spring, MD, USA) combined with a program developed for this study (hirano).

Experimental protocol

The first angiogram was recorded to estimate the baseline diameter of the vessels. Hypercapnia was induced by inhalation of CO2 at 12% mixed in air for 5min. The arterial blood gases were analyzed, and the inhalation was returned to normal room air. An additional angiograph was made at 15 min under normocapnia and arterial blood gases were analyzed. On separate experiments, an infusion pump was connected to the vein catheter and SNP was injected continuously at a flow rate of.....

Measurements of blood gases, glucose osmolarity and insulin

Arterial blood gas tensions and pH were measured with an i-STAT G3 + Cartridge (Abbott Point-of-Care, East Windsor, NJ, USA).

Statistical analysis

Values are expressed as mean ± standard error. One way analysis of variance (ANOVA) was used for the comparison of more than two groups. Post-hoc

comparisons between mean values were made with Scheffe's test. P value <0.05 was accepted as statistically significant.

Results

Table 1 shows the effects of CO_2 inhalation on the average pH, PaO_2, $PaCO_2$ of arterial blood gas from control and GK rats. We determined the initial diameter of each vessel before induction of hypercapnia, there was no statistical difference between the two groups. Baseline diameter for ICA was 232±17.8 um and 278±45.2 um, for Wistar and GK, respectively. For MCA, 211.4 um± 9.9 and 190.0±8.2 um for Wistar and GK, respectively. For perforating baseline diameters were 77.1±4.6 um and 91.5±9.8 um for Wistar and GK, respectively. Figure 1 shows the steady-state responses to hypercapnia of the diameters in ICA, MCA and perforating vessels (Figs. 1A, B and C, respectively) of normal Wistar and GK rats. In ICA we found a significant increase of diameter after 5 min hypercapnia for Wistar rat (126%), GK rat also showed vasodilatation but this failed to be significant (117%). The vessel diameter returned to baseline value after the CO_2 challenge (Fig. 1A). MCA showed a significant increase in diameter in control (142%), GK rat showed 114% dilatation. The vessel diameter returned to baseline value after the CO_2 challenge (Fig 1B). Perforating vessels showed significant vasodilation to hypercapnia in the control group (135%), in the GK group vasodilation was present (112%), but failed to be significant. The vessel diameter returned to baseline value after the CO_2 challenge (Fig 1C).

Nitric Oxide donor, sodium nitroprusside, caused a significant vasodilatation of perforating arteries of both, control and Gk groups (126%-120%, respectively) (Fig 2). ICA and MCA arteries did not show any significant change (Fig 2).

Discussion

This study is the first to directly investigate the effects of chronic hyperglycemia on the response of perforating arteries to hypercapnia and NO donor. We found a significant vasodilatation of rat perforating arteries after hypercapnia with a maximum diameter of approximately 140% of baseline in normal Wistar rats. In contrast, chronic hyperglycemia impaired vasodilatation of perforating arteries in genetically diabetic GK rats. Second, SNP caused a similar vasodilatation of perforating vessels in normal and chronic hyperglycemia, indicating that

endothelium-dependent vasodilatation of perforating arteries may be specifically impaired in chronic hyperglycemia.

Previous experiments have found an intact CO_2 response of cerebral cortical arterioles in the diabetic dogs and STZ-induced diabetic rats (sieber 1993, simpson 1990, wang 1994). In contrast, human studies have (dandona 1978, Griffith 1987, kadoi 2003) observed that diabetic patients failed to respond normally to hypercapnia. Kadoi et al 2003 also suggested that the impaired response was related to severity of diabetes mellitus. The interpretation of clinical studies is complicated by the association of diabetes with microangiopathy and large vessel diseases. Therefore, we investigated the morphological changes in cerebral arteries in brains from 6-month and 12-month-old GK rats prior to this angiographic experiment. It has been reported that diabetes produces thickening of the arterial wall, perivascular and interstitial fibrosis, microaneurysms, arteriolar hyalinosis, and atheromatosis (Muruganandan, velasquez, yu), which could account for the pathogenesis of diabetic cerebrovascular disorders. In 6-month-old GK rats, however, cerebral arteries, including the MCA and perforating vessels did not show such microscopic alterations, nor could we find any significant microscopic changes in the of 12-month-old GK rats (data not shown). Thus, we think that the impaired reactivity to hypercapnia of deeply located vessels including perforating arteries could be due to hyperglycemia, rather than diabetic microangiopathy in GK brains.

In another set of experiments, we have analyzed the effects of hyperglycemia on the blood pressure induced vascular dilatation (autoregulation) of perforating arteries. We have found that autoregulatory responses were reversibly impaired in GK rats (data not shown), which supported the notion that perforating arteries of GK rats had functional loss of endothelium-dependent vasodilatation, rather than structural deficits of cerebral blood vessels. The discrepancy between previous findings and our findings may be related to the differences in experimental methods, including anesthesia, the diabetic animal model used, the severity of hyperglycemia, and the regional differences in CBF regulation. Regional differences in the response of cerebral blood vessels to vasoactive agonists have been specially noted in previous experiments (2, 16 from autoregulation paper).

Several mechanisms have been proposed for the hypercapnia induced cerebrovascular vasodilatation. Hypercapnia requires the development of

extracellular acidosis (kontos 1977, You 1994, Tian 1995). NO is a major mediator of endothelium-dependent relaxation in various vascular beds, and plays an essential role in regulation of the cerebral circulation. Ladecola et al (1994), demonstrated that nitric oxide synthase (NOS) inhibitors attenuated the CBF response to hypercapnia that occurs only at $PaCO_2$ < 100 mmHg. You et al. suggested that the cerebral vasorelaxation elicited by CO_2 was not related with an increase in NOS activity. This might indicate that the cerebral vasodilatation elicited by hypercapnia has NO-dependent and NO-independent components. It is likely that NO plays a role in the response to hypercapnic acidosis and this partly responsible for the increase of cerebral blood flow during hypercapnia (Tian 1995, Iadecola 1992, wang 1992). There is enough evidence of the existence of ATP-sensitive potassium channels (K_{ATP}) in cerebral blood vessels, and therefore their implication in the vasodilatation of cerebral arteries to hypercapnia has also been investigated. Faraci et al (1994) found that glibenclamide attenuated the dilatation of cerebral arterioles in response to a low concentration of acetylcholine and moderate hypercapnia. In diabetes, functional impairment of NO and K_{ATP} channels-mediated vasodilatation have been suggested of pial arterioles and the basilar artery (mayhan 1993, matsumoto 2004). Diabetes is associated with an increased generation of oxygen-derived free radicals in vascular tissues, and reactive oxygen species could influence the structure and activity of K_{ATP} channels (faraci 1998, matsumoto 2004, yu 2002, Niedowicz 2004, erdos 2005). Continuous production of reactive oxygen species produces an impaired vascular response of perforating arteries during chronic hyperglycemia.
There is considerable controversy regarding the effects of NO donors on vascular reactivity. It has been reported that application of intracarotid SNP fails to augment CBF (Young 2002, Joshi 2002), and that the degree of vasodilatation varies in iliac and superior mesenteric arteries (Martines-Nieves 1998). The discrepancy between experiments seems to be inconsistent across animal species and vascular bed examined. However, we could find that application of SNP increased the vascular diameter similarly in control and diabetic rats, suggesting that impaired vasodilatation of perforating arteries to hypercapnia is due to the deficit in NO production/release in vascular endothelium in part during chronic hyperglycemia.
In summary, we could demonstrate the in vivo evidences for the first time that responses of rat perforating arteries to hypercapnia are specifically disrupted

during chronic hyperglycemia. Possible impairment of endothelium-dependent vasodilatation in perforating vessels during chronic hyperglycemia may cause decreased vascular reserve capacity of perforating artery, resulting in the increased ischemic insults and cerebrovascular diseases in diabetes. Further studies are needed to know the cellular mechanism of hyperglycemic impacts on cerebrovascular reactivity.

Acknowledgements

We deeply appreciate Dr. Haruo Yamashita, Dr. Bo Yang, Dr. Yoshikazu Ryu, Dr. Takuya Teranishi, Dr. Abesh K. Bhattacharjee, Dr. Seiji Nakajima, Dr. Akitsugu Morishita, Dr. Masahiro Tamaki, Dr. Takashi Mizobe, Dr. Junji Koyama, Dr. Kazuhiro Tanaka and Dr. Keiji Kidoguchi for their technical assistance. This work was supported by a Research Grant from the Novartis Foundation for Gerontological Research and a Grant-in-Aid for Scientific Research (17500473) from Japan Society for the Promotion of Science (T.S.). Synchrotron radiation experiments were performed at the SPring-8 BL20B2 beamline with the approval of the Japan Synchrotron Radiation Research Institute (Acceptance Nos. 2002A0079-NL2-np, 2002B0312-NL2-np, and 2004A0313-NL3-np).

References

Karapanayiotides T, Piechowski-Jozwiak B, van Melle G, Bogousslavsky J, Devuyst G: Stroke patterns, etiology, and prognosis in patients with diabetes mellitus. Neurology 11; 62(9):1558-62 2004

LeBlanc MH, Huang M, Vig V, Patel D, Smith EE.Glucose affects the severity of hypoxic-ischemic brain injury in newborn pigs. Stroke 1993 Jul;24(7):1055-62.

Groot J, Leeuw FE, Oudkerk M, van Gijn J, Hofman A, Jolles J, Breteler M: Cerebral white matter lesions and cognitive function: the Rotterdam Scan Study. Ann Neurol. 47: 145-151, 2000

(umetani1)Medical and Imaging I (BL20B2). SPring-8 Annual Report 1999: 54-55, 2000

Umetani K, Yamashita T, Maehara N, Tokiya R, Imai S, Kajihara Y: Small-field angiographic imaging of tumor blood vessels in rabbit auricle using X-ray SATICON camera and synchrotron radiation. Proc. 25th Annual Int. Conf. of the IEEE Engineering in Medicine and Biology Society. Cancún: 978-981, 2003

Rieke GK, Bowers DE, Penn P: Vascular supply pattern to rat caudatoputamen and globus pallidus: Scanning electronmicroscopic study of vascular endocasts of stroke-prone vessels. Stroke 12: 840-846, 1981

Hirano M, Yamasaki K, Sakurai T, Kondoh T, Ryu Y, Okada H, Sugimura K, Kitazawa S, Kitazawa R, Maeda S, Katafuchi T, Tamura S: Measurement of blood vessel diameter for angiography using refraction contrast imaging. Igaku Butsuri: 23:157-159, 2003

Muruganandan S, Srinivasan K, Gupta S, Gupta PK, Lal J: Effect of mangiferin on hyperglycemia and atherogenicity in streptozotocin diabetic rats. J Ethnopharmacol 97(3):497-501, 2005

Velasquez MT, Kimmel PL, Michaelis OE 4th: Animal models of spontaneous diabetic kidney disease. FASEB J. 4: 2850-2859, 1990

Yu Y, Ohmori K, Kondo I, Yao L, Noma T, Tsuji T, Mizushige K, Kohno M: Correlation of functional and structural alterations of the coronary arterioles during development of type II diabetes mellitus in rats. Cardiovascular Research 56: 303-311, 2002

Mayhan W, Faraci F: Responses of cerebral arterioles in diabetic rats to activation of ATP-sensitive potassium channels. Am. J. Physiol. (Heart Circ. Physiol. 34): H152-157, 1993

Matsumoto T, Yoshiyama S, Wakabayashi K, Kobayashi T, Kamata K: Effect of chronic insulin on cromakalim-induced relaxation in established streptozotocin-diabetic rat basilar artery. Eur. J. Pharmac. 504: 129-137, 2004

Niedowicz DM, Daleke DL: The role of oxidative stress in diabetic complications. Cell Biochem Biophys. 43: 289-330, 2005

Erdos B, Simandle SA, Snipes JA, Miller AW, Busija DW: Potassium channel dysfunction in cerebral arteries of insulin-resistant rats is mediated by reactive oxygen species. Stroke 35: 964-9, 2004

Faraci FM, Heistad DD: Regulation of the cerebral circulation: role of endothelium and potassium channels. Physiol Rev. 78: 53-97, 1998

ORIGINAL ARTICLE

Radiation Medicine: Vol. 23 No. 2, 89–96 p.p., 2005

Estimation of Contrast of Refraction Contrast Imaging Compared with Absorption Imaging—Basic Approach

Masatsugu Hirano,[1] Katsuhito Yamasaki,[2] Hiroshi Okada,[3] Sohei Kitazawa,[4] Riko Kitazawa,[4] Yoshiharu Ohno,[5] Takashi Sakurai,[6] Takeshi Kondoh,[7] Chiho Ohbayashi,[8] Tetsuro Katafuchi,[9] Sakan Maeda,[4] Kazuro Sugimura,[5] and Shinichi Tamura[10]

Purpose: We discuss the usefulness of the refraction contrast method using highly parallel X-rays as a new approach to minute lung cancer detection. The advantages of refraction contrast images are discussed in terms of contrast, and a comparison is made with absorption images.
Materials and Methods: We simulated refraction contrast imaging using globules with the density of water in air as models for minute lung cancer detection. The contrast intensified by bright and dark lines was compared on a globule with the contrast of absorption images. We adopted the Monte Carlo simulation to determine the strength of the profile curve of the photon counts at the detector.
Results: The obtained contrasts were more intense by two to three digits than those obtainable with the absorption contrast imaging method.
Conclusion: The contrast in refraction contrast imaging was more intense than that obtainable with absorption contrast imaging. A two to three digit improvement in contrast means that it is possible to greatly reduce the exposure dose necessary for imaging. Therefore, it is expected to become possible to detect the interfaces of soft tissues, which are difficult to capture with conventional absorption imaging, at low dosages and high resolution.

Key words: synchrotron radiation, refraction contrast, ray-tracing method, surface dose

Introduction

Remarkable progress has been made in X-ray imaging diagnostic equipment technology. However, conventional absorption imaging has the limitation that its application to the observation of objects with small absorption rate differences is difficult. Expectation is mounting for the development and realization of a next-generation coherent X-ray source similar to that of the laser. Refraction contrast by X-ray (synchrotron radiation) of such a high degree of coherence enables higher contrast imaging, which reflects the object density difference, than that of the absorption imaging method.[1] Thus, it has possibilities for clinical application in the future.[2] Refraction contrast imaging by generating bright and dark lines on the object interface[3] has the effect of improving visibility.[4,5] It was impossible to obtain such images with conventional radiation sources due to their low degree of coherence. However, third-generation radiation sources have enabled highly coherent imaging. The contrast imaging can be applied to the fields of orthopedics, breast cancer, and respiratory systems, among others. In this study, we applied X-ray tracing using Snell's law to the determination of contrast provided by the refraction contrast method and made comparisons with contrast

Received January 5, 2004; revision accepted August 11, 2004.
[1]Department of Electrical Engineering and Information Science, Niihama National College of Technology
[2]Japan Synchrotron Radiation Research Institute
Departments of [3]Urology, [4]Pathology, [5]Radiology, [6]Internal and Geriatric Medicine, and [7]Neurosurgery, Kobe University Graduate School of Medicine
[8]Surgical Pathology Division, Kobe University Hospital
[9]National Cardiovascular Center
[10]Osaka University Graduate School of Medicine
Reprint requests to Masatsugu Hirano, Ph.D., Niihama National College of Technology, 7-1 Yagumo-cho, Niihama, Ehime 792-8580, JAPAN.

This study was partly funded by a research grant (Grant No. 14570899) from the Ministry of Education, Culture, Sports, Science and Technology.

provided by the absorption method. A study has demonstrated that it is possible to obtain high resolution images of lung tissue from excised samples by using refraction contrast imaging by synchrotron radiation.[5] In this study, we examined whether it is possible to obtain high resolution images of live human lung cancer by using this method. For simplification, we used a model that assumes the existence of globules with a density equal to water for evaluation of the method.

Materials and Methods

Lung cancer is known to emerge in the central or peripheral regions, while the regions around tumors are surrounded by air. This paper assumes the existence of globules with an equal density to water in air for simplification of the X-ray imaging simulation.

The refraction index for X-rays is usually expressed $n=1-\delta+i\beta$. Both δ and β are very small. For example, in water, δ is 2.3×10^{-7} and β is 1.2×10^{-10} at 30 keV. Therefore, the refraction index is much larger than the index of absorption β. The real part of the refractive index is smaller than 1.0 but close to 1.0, so the refraction angle is small. In Fig. 1, the refraction angle is $\pi/4 + 0.23\times10^{-6}$ rad (incident angle $\pi/4$ rad).

Parallel monochrome X-rays were illuminated to objects assumed to be soft tissues with diameters of 24 to 1,000 μm and a density of 1.0 in order to obtain their images 0.25 to 10 m behind the samples (refraction) and immediately posterior to them (absorption). The Monte Carlo simulation was applied to the calculation of the travel paths of X-rays along the object surfaces, and absorption is considered in this paper. The number of photons radiated into the pixels of the detector was counted, and the number of counts was interpreted as intensity. The simulation was performed with an energy level of 5 to 60 keV. Thus, determining the density of the globular object, the diameter of the globule, X-ray energy, and the distance between the object and the detector (sample distance) makes it possible to apply the ray-tracing method to the calculation of contrast: C=(Imax−Imin)/(Imax+Imin), (Imax: maximum value of intensity, Imin: minimum value of intensity).

Results

1. Advantages of refraction contrast images over absorption images in terms of contrast

Given that pixel size is 6 μm when the object is in air, bright and dark lines caused by refraction appear in refraction contrast images as explained in Materials and Methods, resulting in contrast intensification (Fig. 1). First, the accuracy of this simulation is tested with

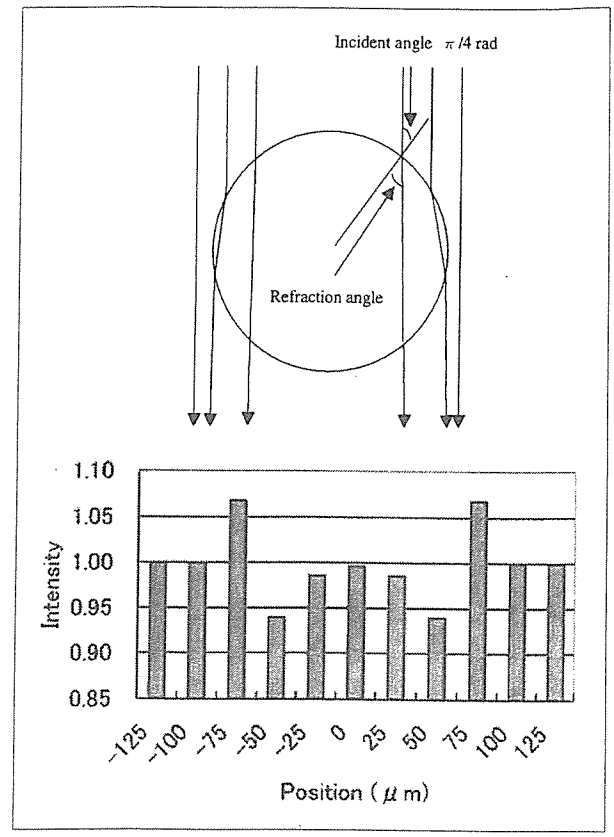

Fig. 1A. Refraction contrast imaging.
The parallel X-ray beams are bent by refraction, generating bright and dark lines outside and inside the boundary lines, respectively. A / B
Fig. 1B. Profile curve of 30 keV X-ray refraction by a globule with a diameter of 100 μm (specific density = 1.0) observed with a detector with a pixel size of 25 μm (the background is normalized to 1.0).

experimental data. The orbit of X-ray photon is calculated using the density and absorption coefficient of the object and surrounding object in this simulation. A sapphire with a diameter of 400 μm in air was scanned with a CCD camera with a pixel size of 6 μm, applying 24.8 keV monochromatic X-rays at BL-28 in SPring-8. The images and profile curves (Fig. 2), obtained at a sample distance of 175 cm with a scanning duration of 6 seconds, were observed to correspond well to the results of calculation by the ray-tracing method. As for contrast, the obtained experimental value was (1.27−0.70)/(1.27+0.70) = 0.29, which corresponds closely to the simulated contrast value of 0.30. For the absorption image, the sample distance was set at 1 cm, and the scanning duration at 6 seconds. Table 1 shows the contrast measured with an absorption image and that obtained in refraction contrast imaging. The refraction image of a 2 mm ball pen refill is shown in Fig. 3B for

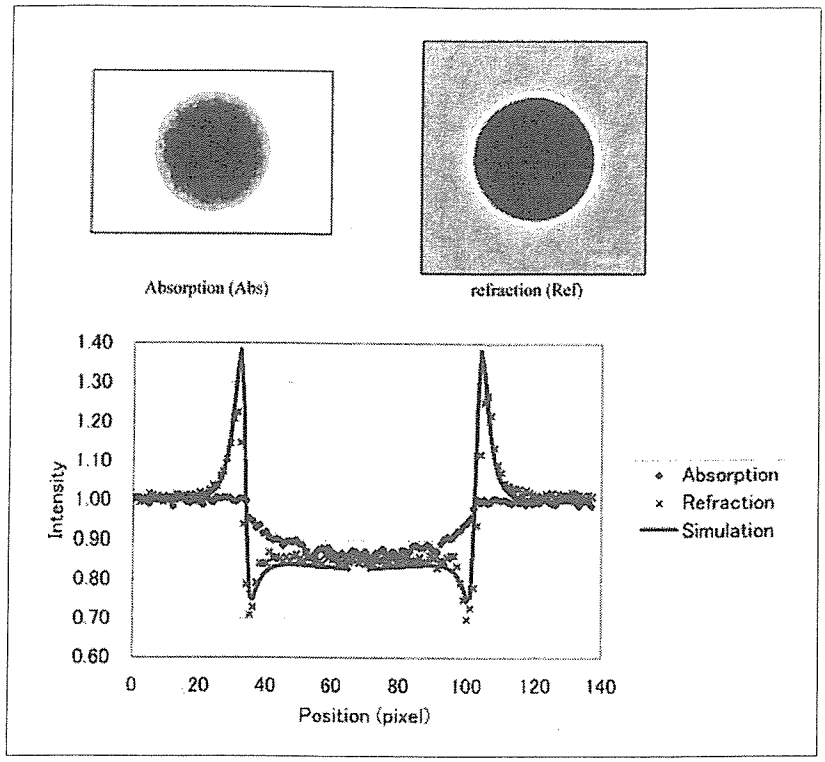

A

B

Fig. 2A. Absorption image and refraction contrast image of a sapphire globule with a diameter of 400 μm at sample distances of 1 cm (abs) and 175 cm (ref).
Fig. 2B. Experimental and calculated data at 24.8 keV, duration 6 seconds.
(1) At a sample distance of 175 cm (red square dots), refraction contrast is observed to be intense.
(2) At a sample distance of 1 cm (blue square dots), the graph is considered to be almost equivalent to the curve of the absorption images.

Table 1. Comparison of contrast of sapphire globule according to imaging method (data obtained by experiment)

Imaging method	Contrast
Absorption	0.07
Refraction	0.29

Table 1 shows that the contrast in refraction contrast images is more intense than that in absorption images. The experiment shows that better contrast is obtainable in refraction contrast images than in absorption images. Figure 2 shows the images referred to in Table 1 and the profile curves along the line through the center.

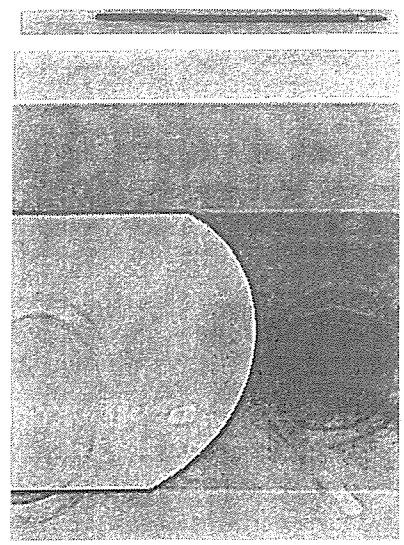

A

B

Fig. 3A. Reference optical image (ball-point pen refill with a diameter of 2 mm).
Fig. 3B. Reference refraction contrast image (ballpoint pen refill with a diameter of 2 mm) at 33 keV.

reference. The absorption at the center of the ball pen refill is approximately 0.05, but the ball pen is clearly recognized. Even printed figures are also clearly recognized.

Figure 4 shows the results of the calculation of the contrasts obtained in refraction contrast imaging and absorption imaging with sample size as the parameter. The energy is 30 keV. The contrast in absorption images decreases almost in proportion to the size of the sample to be observed. Meanwhile, the decrease in the contrast of refraction images is relatively small. Therefore, when the sample size is small, refraction contrast is more advantageous in terms of contrast. Figure 4 also shows the images of globules with diameters of 1 mm, 100 μm, and 24 μm to demonstrate the relative advantage of refraction contrast imaging over absorption imaging in terms of contrast. The contrast in the refraction contrast image is 19 times greater than that in the absorption image even when the globular object has a diameter of 1 mm and 255 times greater and more advantageous by two digits when the diameter of the globular object is 24 μm.

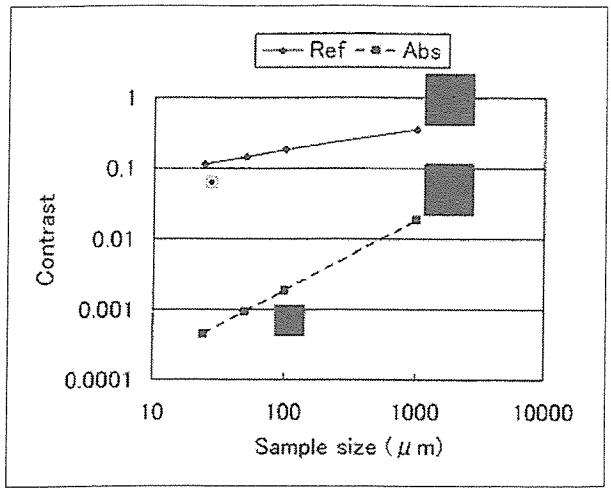

Fig. 4. Sample size dependence of refraction contrast compared with absorption imaging.
The contrast in refraction contrast images is more intense by about two digits than that in absorption images when the conditions of distance between the sample and detector (hereafter referred to as sample distance) are 1 m, X-ray energy is 30 keV, and detector pixel size is 6 μm. X-ray images and their profile curves of intensity of globules 1 mm, 100 μm, and 24 μm are shown. Contrast by the refraction contrast method does not decrease remarkably in relation to sample size reduction. Meanwhile, contrast by the absorption method decreases in reverse proportion to sample size. Therefore, when the size of the observed object is small, higher visibility is achievable with the refraction method. The contrast of a globule with a size of 1 mm is slightly recognizable with the absorption method, and no image can be obtained at all with a globule of smaller size.

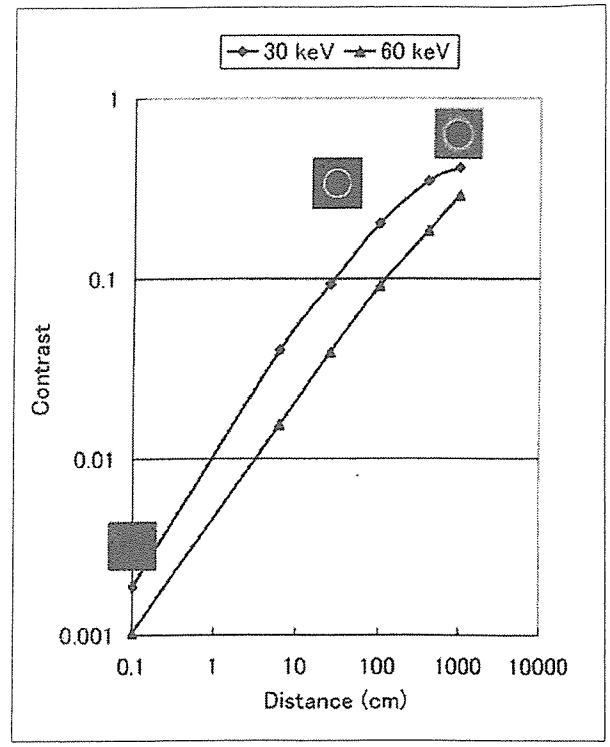

Fig. 5. Sample distance dependence of refraction contrast compared with absorption imaging.
The contrast intensifies in response to the increase in distance with a sample size of 100 μm and detector pixel size of 6 μm. X-ray images of sample distances of 10 m, 4 m, 1 m, 25 cm, 6.25 cm, and 100 μm (absorption image) and their profile curves of intensity are shown. The contrast of the absorption images remains constant independently of the sample distance, and its intensity is between the 15.1 and 282 of that obtained in the refraction images.

2. Intensification of contrast in proportion to sample distance and fading in reverse proportion to energy

(1) Sample distance and contrast

Figure 5 shows the relation between the contrast and sample distance using X-ray energy as a parameter. Figure 5 also shows the images of a 100 μm globule obtained when sample distance is changed from 100 μm (absorption) to 10 m as parameters. Intensity profile curves on a line across the image center are shown next to each image. The contrast is observed to intensify when the increase in sample distance causes bright and dark lines to appear outside and inside the outline of the globule, respectively. The contrast remains constant at 0.0037 for absorption images (distance 100 μm), as shown in Fig. 5.

Figure 5 shows the dependence of contrast on distance to demonstrate that contrast intensifies in response to an increase in distance.

(2) Contrast intensification dependent on energy decrease

Figure 6 shows contrast intensification depending on the decrease in energy from 60 keV to 30 keV and 10 keV to observe a globule with a diameter of 100 μm. The dependence of contrast on energy is shown with the sample distance at 2 m, 1 m, and 25 cm. The contrast fades according to the increase in energy. The longer sample distance along with the lower energy intensifies the contrast. However, the lower energy intensifies the contrast by absorption, diminishing the advantage of refraction.

3. Change in contrast according to globule-detecting resolution in air and sample size

(1) Contrast intensification in proportion to resolution of the detector

Figure 7 shows how the contrast in the image of a globule with a diameter of 100 μm intensifies according to the reduction in pixel size from 25 to 6 to 1 μm. Figure 7 also shows an image and profile curve for each pixel size, and the relation between contrast and pixel size

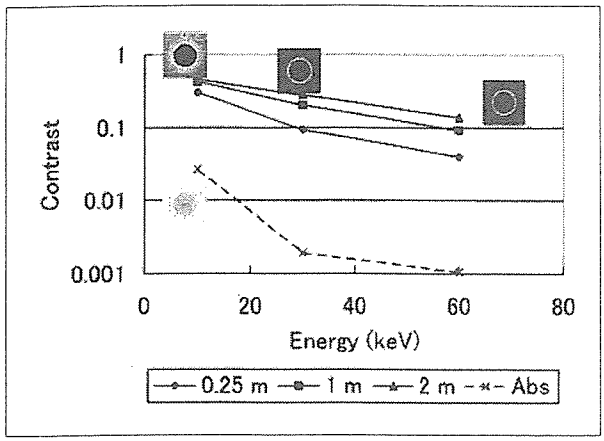

Fig. 6. Energy and sample distance dependence of refraction contrast compared with absorption imaging.
X-ray images of sample distance 1 m, 100 μm (absorption image) and their profile curves of intensity are shown. Figure 6 shows that, with sample distance constant, energy reduction improves contrast. This effect is enhanced as sample distance increases.

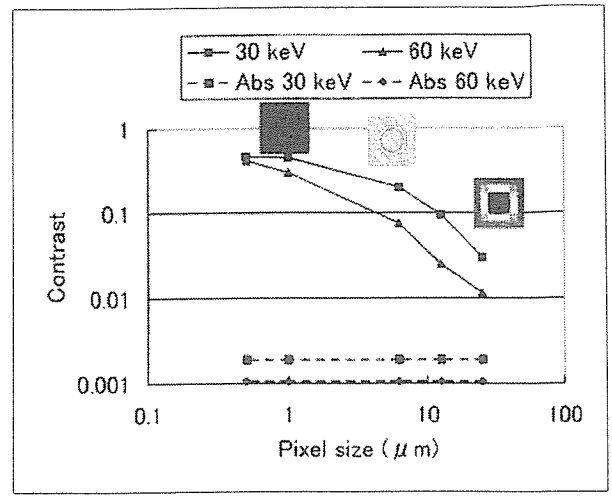

Fig. 7. Detector pixel size dependence on refraction contrast.
X-ray images of pixel size of 25 μm, 6 μm, and 1 μm and their profile curves of intensity are shown. These images show that the reduction in pixel size intensifies the contrast.

(including pixel size 0.5 μm). While the number of photons necessary to measure refraction contrast images increases in inverse proportion to detector pixel size Px, the reduction in pixel size makes the difference between bright and dark lines remarkable, resulting in the intensification of contrast. Therefore, the total number of necessary photons increases only moderately. Note, however, that the decline in detector efficiency is ignored here. Noise has an important role for contrast in finite photon numbers. However, because the aim of this study was to estimate contrast, noise is ignored here. To exploit the advantages of the refraction contrast method, it is necessary to reduce the pixel size of the detector.

As can be seen in the images shown in Fig. 7, the refraction effect makes the difference between bright and dark lines remarkable in response to the reduction in pixel size. Because of this, contrast is also intensified, as shown in the profile curve (30 keV, sample distance fixed constant at 1m).

(2) Invariance of contrast against sample size reduction

Figure 8 shows the change in contrast in response to the reduction in sample size for each detector pixel size at an energy level of 30 keV. We have already shown in Result 1 that contrast remains constant against the reduction in sample size. It is shown here that refraction contrast is more advantageous than absorption contrast to observe minute objects.

4. Dependence of the contrast on difference in density

Figure 9A and 9B show images of 100 μm globules with specific gravities of 1.1, 1.01, and 1.001 placed as

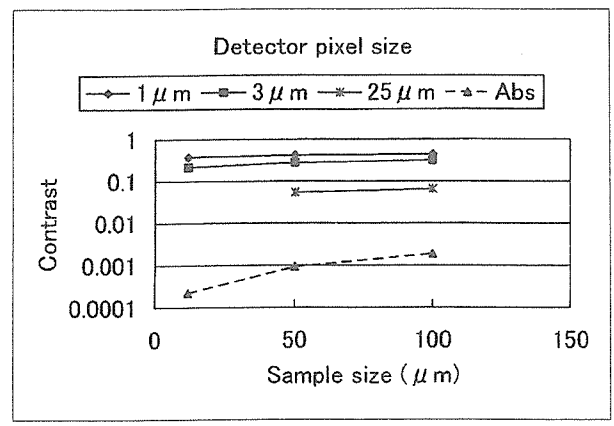

Fig. 8. Sample size and pixel size dependence on refraction contrast.

in Fig. 10 in the center of a water layer 200 μm thick to study the differences in refractive index. Figure 9A and 9B also shows the dependence of contrast on pixel size and density ratio, which are also shown in Tables 1 and 2. The X-ray energy is set at 60 keV and 5 keV. It is advantageous in terms of contrast to keep energy low and pixel size small, because it is difficult to detect refraction between small density differences in high enregy.

The tables suggest that the contrast-intensifying effect caused by refraction is strong where a large density difference is present, while the effect diminishes with a density difference as small as 0.1%. Since the reduction in detector pixel size to 6 μm makes it possible to obtain contrast of 0.04 at 5 keV, even where a density difference

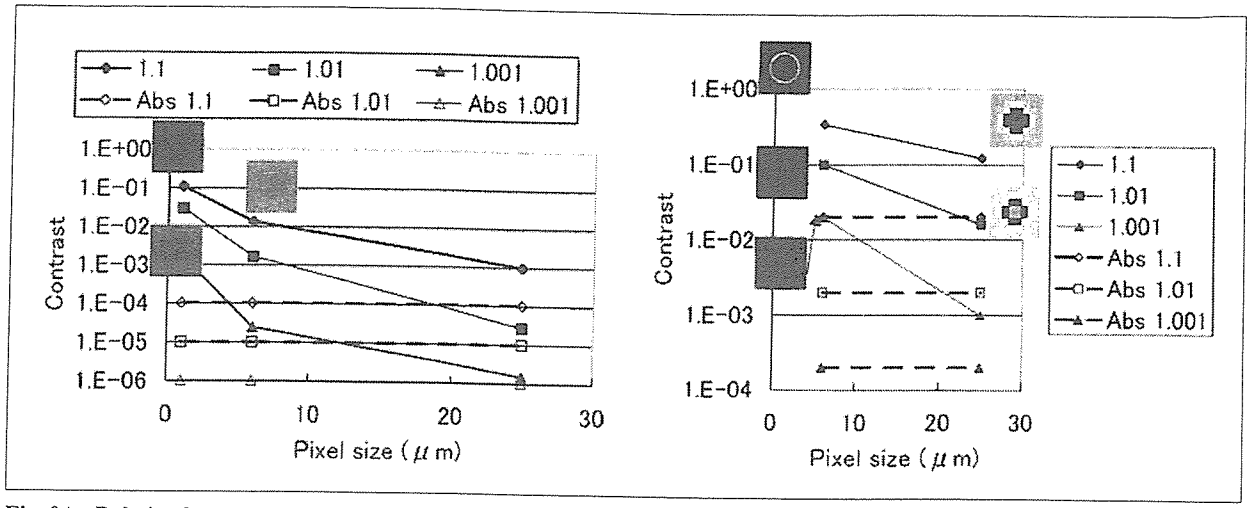

Fig. 9A. Relation between contrast and pixel size with various density differences at an X-ray energy level of 60 keV.
(1) Images are hard to visualize by absorption at 60 keV with the density difference at 1.1, 1.01, or 1.001.
(2) No good contrast is obtainable with a pixel size of 25 μm, thus making visualization by refraction difficult, too. Even with a pixel size of 6 μm, visualization is possible only when the density difference is 1.1. When pixel size is 1 μm, contrast remains at 0.031 down to a density difference of 1.01, thereby making visualization somehow possible.
Fig. 9B. Relation between contrast and pixel size with various density differences at an X-ray energy level of 5 keV.
(1) The contrast in absorption images is 0.04 at 5 keV when the density difference is 1.1, making visualization possible. When the density difference is 1.01 or 1.001, the contrast is 0.002 or 0.0002, making visualization difficult.
(2) A contrast of 0.12 or 0.017 is obtained by refraction with pixel size at 25 μm when the density difference is 1.1 or 1.01. Thus, visualization by refraction becomes possible as shown above. With the density difference at 1.001, the obtained contrast is 0.001, making visualization difficult. With the density difference at 6 μm, the obtained contrast is 0.02 even at a density difference of 1.01, making visualization possible. With the density difference at 1 μm, the obtained contrast is 0.16, resulting in a good image. Table 2 summarizes visualization performance.

as small as 0.1 is present, the contrast is still considered to be measurable. Moreover, with the pixel size at 1 μm, it is possible to obtain sufficient contrast of 0.031.

To intensify contrast by the refraction contrast method in relation to density difference, it is necessary to reduce the pixel size of the detector. Contrast intensifies in inverse proportion to pixel size. Yet, with the density difference at 1.001, the contrast obtainable with a pixel size of 1 μm is as small as 0.0035. It takes a density difference of at least 1.01 to visualize the border (Fig. 9A).

In this case, even with a small density difference, better contrast is obtained than that obtainable at 60 keV. The reduction in pixel size to as small as 6 μm improves contrast by two digits, making it 100 times more intense than that obtainable by absorption (Fig. 9B).

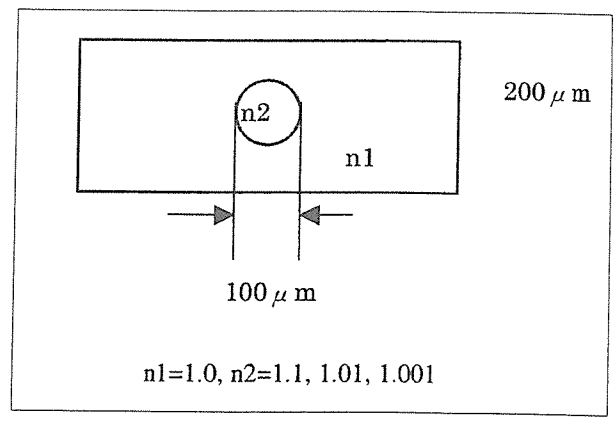

Fig. 10. Schematic diagram of a tabular region 200 μm thick with a density of 1.0 containing a globular region with a diameter of 100 μm (density n2: 1.1, 1.01, and 1.001) at its center.
See Figs. 9A and 9B for images of the globular region shown in Fig. 10 by the absorption method and the refraction contrast method, respectively.

DISCUSSION

In this study, we examined the contrast ratio in refraction contrast imaging and absorption contrast imaging. According to Reference 6, when the absorption method is applied, the number of necessary photons changes in proportion to X^{-4}, where X denotes the size of the object to be identified. The number of necessary photons increases to detect smaller obstacles. Thus, in the absorption method, the dose reaches as high as 160 Gy at 30 keV when detecting a globule with a diameter of

Table 2. Contrast at 60 keV, sample size 100 μm

Density	Pixel size	Contrast by absorption	Contrast by refraction	Ref/abs
1.1	25	0.00011	0.001	9.5
	6		0.014	129
	1		0.11	1048
1.01	25	1.0E-05	2.8E-5	2.7
	6		0.0017	160
	1		0.031	2961
1.001	25	1.0E-06	1.6E-6	1.5
	6		2.5E-5	24
	1		0.0018	1699

Table 3. Contrast at 5 keV

Density	Pixel size	Contrast by absorption	Contrast by refraction	Ref/abs
1.1	25	0.02 (>)	0.12 (>)	6
	6		0.34 (>)	17
	1		0.46 (>)	23
1.01	25	2.0E-03 (<)	1.6E-2 (>)	8
	6		0.10 (>)	50
	1		0.40 (>)	198
1.001	25	2.0E-04 (<)	0.001 (<)	5
	6		0.020 (>)	100
	1		0.016 (>)	775

Visualization performance is indicated in parentheses: (>) means a contrast of 0.01 and over, while (<) means contrast below that. Sample size = 100 μm.

100 μm with detector pixel size at 25 μm. Meanwhile, the contrast provided by the refraction contrast method is 19 times more intense than that obtainable with the absorption imaging method, and, with the pixel size at 6 μm, 105 times more intense, making detection even more advantageous. Further reduction in sample size to 50 μm and then to 24 μm diminishes the contrast obtained by absorption to 1.88×10^{-3} and 9.01×10^{-4}, respectively, while the contrast provided by refraction remains almost constant.

In absorption imaging, given that the S/N ratio at which objects of the same size are detected is kept constant, the necessary dose (number of photons) is reduced at least in proportion to Px^{-2}, where Px denotes pixel size. Conversely, since the contrast between refracted bright and dark lines intensifies in response to pixel size reduction in refraction imaging, the necessary dose is not reduced in proportion to Px^{-2}. The smaller the pixel size, the sharper the image, resulting in more intense contrast (see Fig. 7). In this respect, the refraction contrast imaging method is expected to be applied to next-generation X-ray imaging that has the advantages of high resolution and low exposure dosages. Refraction contrast imaging can demonstrate the effectiveness of its advantages in the X-ray energy range between 30 and 60 keV only when the material density difference of the interface is large. Therefore, refraction contrast is effective for the detection of locations where a large material density difference is present, such as the interface between air and biological materials or that between bones and biological materials.

However, if a detector pixel size as small as 1 μm were available at energy as low as 5 keV, good refraction contrast could be obtained even at a density difference as small as 0.1%. Although no detectors with a pixel size of 1 μm exist in reality, it would be highly useful if they did. Realistically, it might be possible to realize the advantages of such a pixel size by using films with a resolution of 1 μm. Still, the application of a low X-ray energy of 5 keV to the human body would be impractical. Moreover, the effects of multiple scattering have not been quantitatively dealt with in past discussions. Since achievable refraction contrast is expected to be lower than that obtained by calculation because of scattered

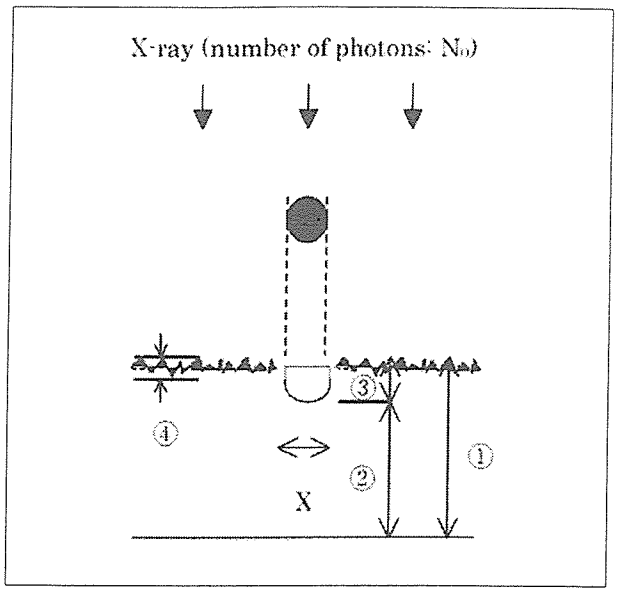

Fig. 11. Absorption imaging: schematic diagram of parallel X-ray irradiation on a globule.

radiation, experimental verification is needed.

In addition, it would be necessary to take into consideration that high X-ray energy results in low efficiencies of detectors. In Fig. 11, Item ① is the number of X-ray photons when no object is present. X indicates the diameter of an object. Item ③ is the reduction in the number of photons due to absorption by the object, Item ② indicates the number of photons penetrating the object, and Item ④ indicates the variation of the background. Given that the water attenuation coefficient in Fig. 11 is μ, Item ③, is expressed by $k = N_0\{1-\exp(-\mu X)\}/N_0$.

In the case of refraction contrast imaging, given that the peak intensity of a bright line is N (bright), the lowest intensity of a dark line is N (dark), and the number of photons in the background is N_0, k is defined as {N (bright) – N (dark)}/N_0.

Here, let R be efficiency, then the required dose (number of photons) is expressed by N_0 (min.) = $8/(Rk^2)$ in Reference 6, and the dose becomes effective both in absorption and refraction with the same factor. The radiation dose of refraction contrast imaging decreases compared with those of absorption imaging with same efficiency of detector.

Another issue to be considered is the speckle effect caused by the overlapping of images of objects with long depths. This will be discussed in another paper.

In this paper, we discussed the contrast-intensifying effect of the refraction contrast method, based on calculations obtained by the ray-tracing method. Using experimental data for comparison, we have demonstrated that the ray-tracing method is sufficient to reproduce the contrast obtained by the refraction contrast method. We have shown that the advantage of refraction imaging becomes greater in terms of contrast ratio than that of conventional absorption imaging in inverse proportion to the size of the object and the pixel size of the detector. We have also shown that, where a small detector pixel size is available at low energy, good refraction contrast can be obtained even when the density difference is small. A two to three digit improvement in contrast means that it is possible to greatly reduce the exposure dose necessary for imaging. The refraction contrast method is expected to be applied to next-generation clinical X-ray imaging.

ACKNOWLEDGEMENT

We are grateful to Professor Masami Ando of the High Energy Accelerator Research Organization and Dr. Masami Torikoshi of the National Institute of Radiological Sciences for their comments, and to Dr. Yoshiki Kohmura and Dr. Yasuhiko Imai of SPring-8, Dr. Kunio Shinohara for their discussions and comments. We would like to express our deep appreciation for the encouragement and inspiration of the late Dr. Minoru Oda. This study was partly funded by a research grant (Grant No. 14570899) from the Ministry of Education, Culture, Sports, Science and Technology.

REFERENCES

1) Snigirev A, Snigireva I, Kohn V, Kuznetsov S, Schelokov I. On the possibilities of x-ray phase contrast microimaging by coherent high-energy synchrotron radiation. *Review of Scientific Instruments,* 66: 5486–5492, 1995.
2) Arfelli F, Bonvicini V, Bravin A, *et al.* Mammography with synchrotron radiation: phase-detection techniques. *Radiology,* 215: 286–293, 2000.
3) Yagi N, Suzuki Y, Umetani K, Kohmura Y, Yamasaki K. Refraction-enhanced x-ray imaging of mouse lung using synchrotron radiation source. *Med Phys,* 26: 2190–2193, 1999.
4) Yamasaki K, Hirano M, Nagai H, *et al.* Refraction-enhanced X-ray imaging using synchrotron radiation source. *Technical Report of IEICE,* MI2001–46: 15–20, 2001.
5) Kono M, Ohbayashi C, Yamasaki K, *et al.* Refraction imaging and histologic correlation in excised tissue from a normal human lung: preliminary report. *Acad Radiol,* 8: 898–902, 2001.
6) Hirano M, Yamasaki K, Torikoshi M, *et al.* Evaluation of radiation dose required for angiography. *AIP Conference Proceedings,* 705 (1): 1031–1034, 2004.